

Manuscript version: Author's Accepted Manuscript

The version presented in WRAP is the author's accepted manuscript and may differ from the published version or Version of Record.

Persistent WRAP URL:

<http://wrap.warwick.ac.uk/127098>

How to cite:

Please refer to published version for the most recent bibliographic citation information. If a published version is known of, the repository item page linked to above, will contain details on accessing it.

Copyright and reuse:

The Warwick Research Archive Portal (WRAP) makes this work by researchers of the University of Warwick available open access under the following conditions.

© 2019 Elsevier. Licensed under the Creative Commons Attribution-NonCommercial-NoDerivatives 4.0 International <http://creativecommons.org/licenses/by-nc-nd/4.0/>.



Publisher's statement:

Please refer to the repository item page, publisher's statement section, for further information.

For more information, please contact the WRAP Team at: wrap@warwick.ac.uk.

1 Experimental and numerical investigation of the interaction of
2 the first four SH guided wave modes with symmetric and non-
3 symmetric discontinuities in plates

4
5 Alan C. Kubrusly^a, Jean Pierre von der Weid^a and Steve Dixon^b

6
7 ^{a.} Centre for Telecommunication Studies, Pontifical Catholic University of Rio de Janeiro, Rio de
8 Janeiro, 22451-900, Brazil; alan@cpti.cetuc.puc-rio.br

9 ^{b.} Department of Physics, University of Warwick, Coventry, CV4 7AL, UK; S.M.Dixon@warwick.ac.uk

10
11 ***Abstract***—The interaction of the SH₀, SH₁, SH₂ and SH₃ guided wave modes on a
12 metal plate with a thickness discontinuity is numerically and experimentally investigated.
13 Two different geometries were evaluated, namely symmetric and non-symmetric
14 discontinuities, relative to the plate longitudinal mid-plane. Experiments were performed
15 with periodic permanent magnet array EMATs as transmitters and receivers. Mode
16 separation in transmission and reception was experimentally and numerically performed
17 by dual transduction and by modal decomposition post-processing techniques,
18 respectively. The reflection and transmission coefficients at the discontinuity for each of
19 the investigated SH modes was calculated. It has been experimentally confirmed that
20 when interacting with symmetric discontinuities, only modes that share the same
21 symmetry as the incident mode are created by mode conversion, whereas mode
22 conversion to modes of different symmetry can occur with non-symmetric discontinuities.
23 Experimental and numerical data show good agreement, revealing that the higher the
24 order of the incident mode, the more complex the behaviour of the reflection coefficient
25 is, as a function of the discontinuity depth. For the same incident mode, symmetric
26 discontinuities impose less complexity than non-symmetric ones.

27 ***Keywords***—SH guided waves; mode conversion; PPM EMAT; wall thinning; reflection
28 and transmission coefficients; symmetric discontinuities.

29 **1. Introduction**

30 Ultrasonic guided waves are used widely for detecting defects, such as cracks and corrosion,
31 in plates or pipes [1-4]. Non-destructive defect characterisation by means of ultrasonic guided
32 waves relies on detecting the forward-scattered or back-scattered field produced by a guided
33 wave mode that impinges on a defect [5]. Since the scattered field depends on the defect shape
34 and size [6-8], comprehensive knowledge of the interaction of guided wave modes with defects
35 is of great interest. Shear Horizontal (SH) waves are a family of guided waves that present in-
36 plane particle motion, perpendicular to the direction of propagation. SH waves present some
37 advantages, such as no energy leakage to surrounding non-viscous fluids, and they also have
38 relatively simple dispersion relations compared to other guided wave modes. SH waves can be
39 generated efficiently and detected in metallic samples with electromagnetic acoustic
40 transducers (EMAT) [9-11].

41 Several authors investigated the interaction of SH guided wave in plates and torsional waves
42 in pipes with notch and thickness discontinuities, that are commonly used to crudely describe
43 corrosion-like defects [12-17]. Quantitative analysis is usually performed by calculating the
44 reflection and transmission coefficient of the scattered waves [6, 12-14, 16-21]. Depending on
45 the product of frequency and plate thickness, several SH modes can propagate, which can make
46 interpretation of SH waves complicated. As a result, experiments are often restricted to the so-
47 called low frequency-thickness regime, where only the SH₀ mode or the T(0,1) mode, can
48 propagate, in plates or pipes, respectively [6, 8, 12-14, 16, 18, 21-25]. Demma et al.
49 investigated the scattering of the SH₀ mode from rectangular notches in plates [12], and of the
50 torsional mode T(0,1) in pipes [13], where both reflection from the notch leading edge and
51 transmission away from the defect were analysed. The reflection and transmission from step-
52 up and step-down thickness changes at low frequency were well approximated by simply
53 considering an analogy of the thickness reduction with an acoustic impedance change. Wang

54 et al. [24] numerically calculated the reflection and transmission coefficients for the
55 circumferentially propagating SH0 mode with slots in pipes, that were used to simulate finite
56 length axial cracks. More realistic defect geometries were also investigated, such as three-
57 dimensional elliptical defects [22], tapered edge defects [6] and irregular shapes [8, 23, 26] and
58 also overlap joint of plates [25].

59 In the high frequency-thickness regime, the interaction of guided waves with defects is more
60 complicated, since the scattered waves may be composed of several propagating SH modes
61 due to mode conversion [7, 15, 17, 19, 20]. Nurmalia et al. [7, 15] experimentally analysed the
62 SH0 and SH1 modes in plates and the T(0,1) and T(0,2) modes in pipes [27] with gradual
63 thickness reduction sections, showing that the interaction with defects depends on the thickness
64 reduction rate. Recently, Kubrusly et al. [20] calculated the coefficients for reflection and
65 transmission, for a large range of wall thinning depths and edge angles in plates, in a frequency-
66 thickness product region where both the SH0 and SH1 were able to propagate. Kubrusly
67 experimentally proved that mode conversion behaviour is complex, resulting in non-monotonic
68 reflection and transmission coefficients. In the low frequency-thickness regime, the reflection
69 and transmission coefficients tend to behave monotonically as a function of the discontinuity
70 depth [12, 14, 16, 24].

71 Most published work considers discontinuities located on one of the surfaces of the plate,
72 rather than being symmetrically present on both surfaces. Nevertheless, the interaction with
73 symmetric discontinuities has also attracted the attention of researchers. Pau et al. analysed the
74 reflection and transmission [16, 17] coefficients for the incident SH0 mode in both the low and
75 high frequency-thickness regime in a plate with symmetric and non-symmetric notches. An
76 analytical model was used in order to evaluate the coefficients as a function of the discontinuity
77 depth and was further compared with finite element simulations. In the low-frequency
78 thickness regime, no significant difference between the symmetric and non-symmetric

79 discontinuities was observed [16, 17], whereas in the high-frequency regime [17] symmetric
80 and non-symmetric discontinuities behave differently. It was observed that conversion to any
81 propagating mode is allowed for non-symmetric discontinuities, whereas only symmetric
82 modes were produced when a symmetric mode interacts with a symmetric discontinuity. Pau
83 and Achillopoulou [19] extended their analysis for different geometries of the thinner section.
84 Guided wave interactions with rectangular and elliptic profile notches and voids in the middle
85 of the plate's cross-section were numerically simulated. Symmetric notches and voids allowed
86 conversion to symmetric modes only, whereas non-symmetric notches and voids permitted
87 mode conversion to modes of either symmetry. In both cases, the coefficients depend on the
88 notch or void depth. Interestingly, for both low and high frequency-thickness cases, symmetric
89 notches and voids in the middle of the plate present the same coefficient's values, and the
90 elliptical and the rectangular notches showed similar results. Yan and Yuan [28] numerically
91 analysed the conversion from the evanescent SH1 mode from either symmetric or non-
92 symmetric apertures, such as a thinner section of a plate, into propagating modes in the full
93 thickness section. In the former, the evanescent SH1 mode was converted only to the
94 propagating SH1 mode, whereas in the latter, it was converted to either the propagating SH0
95 or SH1 modes.

96 The aforementioned papers show that the characteristics of the scattered waves depend on
97 whether a discontinuity is symmetric or not; a symmetric mode can only be mode converted to
98 symmetric modes when interacting with a symmetric discontinuity. However, no experimental
99 validation was performed and only the propagating symmetric SH0 mode was used as the
100 incident mode; the interaction of higher-order SH modes with symmetric or non-symmetric
101 discontinuities was not investigated. It is indeed non-trivial to experimentally quantitative
102 evaluate such phenomena, due to mode mixing of the several possible propagating modes,
103 which render interpretation of the received signal complicated. In this paper, we address the

104 interaction of the first four SH guided waves modes with thickness reduction discontinuities in
 105 plates in two different shapes, namely non-symmetric and symmetric, in order to analyse the
 106 mode conversion phenomena of symmetric and antisymmetric modes in these cases. Both
 107 experiments and numerical simulation were performed. Quantitative experimental data was
 108 obtained using the dual excitation and reception technique [29], which enables the calculation
 109 of the reflection and transmission coefficients for the discontinuity, considering all mode
 110 conversion possibilities.

111 2. SH guided waves

112 Shear horizontal guided waves have vibrational displacement perpendicular to the
 113 propagation direction and parallel to the plate's surface [30] which is given by:

$$u_z(x, y, t) = A_n U_n(y) e^{j(\omega t - \kappa_n x)}, \quad (1)$$

114 where x is the propagation direction, y is the coordinate of the plate thickness, z is the
 115 polarization direction, ω is the angular frequency, n is the mode order, κ_n , A_n and $U_n(y)$ are
 116 the wavenumber, amplitude and displacement profile of mode n , respectively. SH modes are
 117 usually classified as symmetric and antisymmetric according to their displacement profile,
 118 which can be described by:

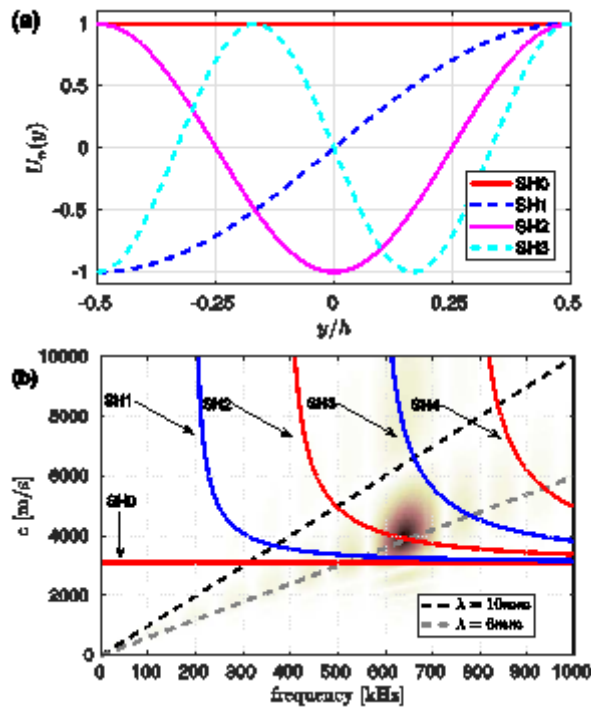
$$U_n(y) = \cos(n\pi y/h + 3n\pi/2), \quad (2)$$

119 where h is the plate thickness. Symmetric modes have equal displacement at both surfaces ($y =$
 120 $\pm h/2$), whereas antisymmetric modes have displacement with the same absolute value, but of
 121 opposite sign at each surface. Even-order modes are symmetric, whereas odd-order modes are
 122 antisymmetric. Fig. 1(a) shows the displacement profile for modes SH0 to SH3. Apart from
 123 the fundamental zero-order SH0 mode, all other higher-order modes are dispersive and are only
 124 able to propagate for a frequency-thickness product above a cut-off value. At a fixed frequency,

125 higher-order modes cannot propagate if the plate's thickness is below the cut-off thickness
 126 given by:

$$h_{\text{cut-off}} = n c_T / 2f , \quad (3)$$

127 where c_T is the transverse wave speed and f is the frequency. For dispersive modes, the phase
 128 and group velocities depend on the frequency. Fig. 1(b) show the dispersion curves of SH
 129 guided wave modes for an 8 mm thick aluminium plate.



130

131 Fig. 1. (a) SH modes displacement profile. Continuous and dashed lines represent symmetric and antisymmetric
 132 modes, respectively. (b) Phase velocity dispersion curves of an 8 mm thick aluminium plate, red lines represent
 133 symmetric modes and blue lines, antisymmetric modes. The dashed lines represent a constant wavelength of 10
 134 mm and 6 mm. The operating region for generation of the SH2 mode, centred at frequency 649 kHz and at 6 mm
 135 wavelength is shown behind the dispersion curves.

136

137

138 An ultrasonic wave carries energy whose power density is given by the vector [31]:

$$\mathbf{s} = -\frac{1}{2} \mathbf{v}^* \cdot \boldsymbol{\sigma} , \quad (4)$$

139 where \mathbf{v} is the particle velocity vector, $\boldsymbol{\sigma}$ is the stress tensor and the asterisk means complex
 140 conjugate. For an SH guided wave mode, the relevant components of \mathbf{v} and $\boldsymbol{\sigma}$ can be obtained
 141 from Eq. (1), yielding, respectively:

$$v_z = j\omega A_n U_n(y) e^{j(\omega t - \kappa_n x)} , \quad (5)$$

142

$$\sigma_{xz} = -j\mu\kappa_n A_n U_n(y) e^{j(\omega t - \kappa_n x)} . \quad (6)$$

143 where μ is the second Lamé constant. Therefore, the power density along the propagating
 144 direction for mode n is:

$$S_n = \frac{1}{2} \mu \omega \kappa_n U_n^2(y) |A_n|^2 , \quad (7)$$

145 and the power per unit width in the plate is given by the integral of S_n over the plate's height,
 146 which can be written as

$$P_n = E_n |A_n|^2 , \quad (8)$$

147 where E_n is here called the power level of the mode n , whose value is:

$$E_n = \frac{1}{2} \mu \omega \kappa_n \int_{y=-h/2}^{h/2} U_n^2(y) dy . \quad (9)$$

148 SH guided waves can be generated and detected with periodic permanent magnet (PPM)
 149 array EMATs, which consist of an array of magnets with an elongated spiral or “racetrack” coil
 150 underneath the PPM array [9, 10, 32]. The spacing or pitch of the magnets in the PPM EMATs
 151 imposes a nominal wavelength on the generated waves. Fig. 1(b) shows the nominal
 152 wavelength of a 10 mm and a 6 mm probe (straight dashed lines), superposed on the dispersion
 153 curves of the SH modes. The optimum excitation of a particular mode is achieved at the
 154 frequency where the wavelength line crosses the dispersion curve of this mode. Table I shows

155 the optimum excitation frequency to generate SH modes, from order 0 to 3, used in this paper.
156 However, due to the finite number of magnets in the array, the EMAT has a finite wavelength
157 bandwidth of waves that can be excited [9]. Similarly, the excitation electric current applied to
158 the coil produces a temporal bandwidth. The intersection of both bandwidths defines a region
159 of operation, in which SH waves can be generated or received [3, 20, 29]. As an example, Fig.
160 1(b) shows the operating region for generating the SH2 mode, with a 3 cycle, 6 mm wavelength
161 probe, using an 8 cycle tone burst at 649 kHz, which is the optimum frequency for SH2
162 generation. One can observe that the dispersion curve of the SH2 mode crosses the centre of
163 this region.

164 **Table I. Optimum excitation frequency for SH modes in an 8 mm thick aluminium plate and the possible mode**
165 **conversions with their cut-off thicknesses; the value in parentheses means the maximum discontinuity relative depth**
166 **(d/h) for a transmitted mode to propagate.**

Nominal λ (mm)	Generated mode	Opt. excitation freq. (kHz)	Cut-off thicknesses of the possible mode conversions			
			SH0	SH1	SH2	SH3
10	SH0	311	0 mm	5.00 mm (37.5 %)	10.0 mm (-)	15.0 mm (-)
	SH1	367	0 mm	4.24 mm (47.0 %)	8.48 mm (-)	12.7 mm (-)
	SH2	498	0 mm	3.12 mm (61.0 %)	6.25 mm (21.9 %)	9.37 mm (-)
	SH3	662	0 mm	2.35 mm (70.6 %)	4.70 mm (41.3 %)	7.05 mm (11.9 %)
6	SH1	554	0 mm	2.81 mm (64.9 %)	5.62 mm (29.8 %)	8.43mm (-)
	SH2	649	0 mm	2.40 mm (70.0 %)	4.80 mm (40.1 %)	7.19 mm (10.12 %)
	SH3	782	0 mm	1.99 mm (75.1 %)	3.99 mm (50.3 %)	5.97 mm (25.4 %)

167
168 When a guided wave mode impinges upon some feature in the plate, such as a section with
169 reduced thickness, the scattered field may be composed of several modes, i.e. the incident mode
170 may suffer mode conversion either as reflection from the discontinuity or transmission to the
171 thinner section [7, 15, 17, 19, 20]. Mode conversion to a propagating mode can arise only if its
172 cut-off thickness, given by Eq. (3), is less than the plate's thickness. Table I also shows the
173 possible converted modes, and their cut-off thickness, for incident modes from zero to third

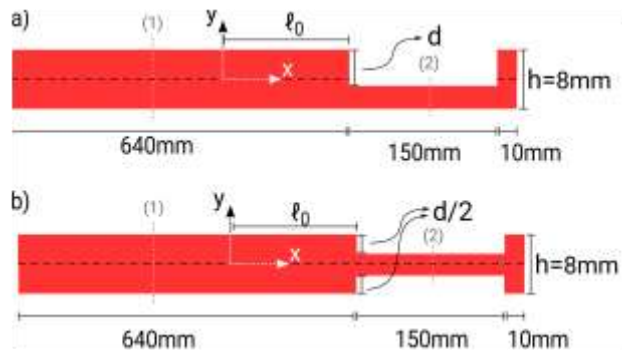
174 order, in an 8 mm thick aluminium plate. Cells marked with a dash mean that the mode
175 conversion is not possible, due to the high cut-off thickness of the converted mode. It is worth
176 highlighting that mode conversion with transmission to a thinner section of the plate can only
177 happen if its remaining thickness is higher than the respective cut-off thickness; the percentage
178 values in parentheses in Table I, give the maximum depth to original thickness value that a
179 thinner section may have for a transmitted mode propagate.

180 **3. Numerical and experimental investigation**

181 *3.1. Experimental setup and geometry*

182 In order to analyse the interaction of SH waves, aluminium plates were machined with two
183 types of discontinuity, namely symmetric and non-symmetric. In this case, a non-symmetric
184 sample presents a discontinuity at a single surface with depth d , whereas a symmetric one
185 presents discontinuity at both surfaces of the plate at the same longitudinal position, with each
186 of their depths equal to $d/2$. Thus the total thickness reduction equals d in both cases. The test
187 samples were 8 mm thick, 800 mm long and 250 mm wide aluminium plates. The geometry of
188 the samples is shown in Fig. 2: the plate's plane lies in the x - z plane (thickness in the y -
189 direction, length in the x -direction), the origin is defined as the position where the generating
190 transducer is placed. The discontinuity is 150 mm long, ending 10 mm away from the right end
191 of the plate, as shown in Fig. 2. The short section at the rightmost end of the plate plays no role
192 in this study; this section had to remain with the original thickness in order to clamp the plates
193 for machining. Here, only reflection and transmission at the leading edge of the discontinuity
194 were investigated, transmission or reflection at the far end of the section was not analysed. The
195 section at the left of the discontinuity was set to be long enough (640mm) in order to allow
196 flexibility for the positioning of transducers. For each type of sample, three different total

197 depths were machined, 2 mm, 4 mm and 6 mm, corresponding to 25 %, 50 % and 75 % of the
 198 original thickness, respectively.

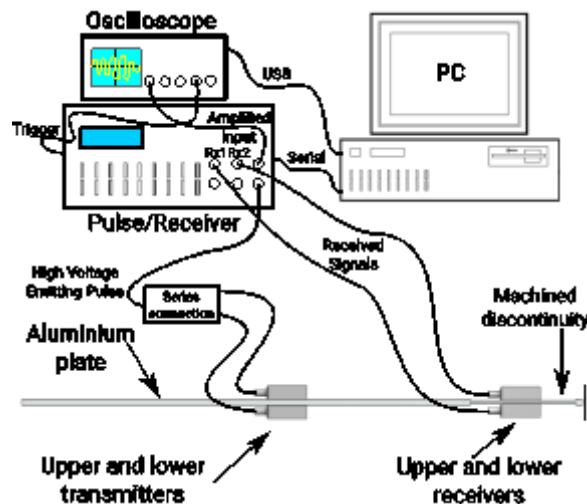


199

200 Fig. 2. Plate and discontinuity geometry. (a) Non-symmetric discontinuity. (b) Symmetric discontinuity.

201

202 Experiments were performed using a RITEC © RPR-4000 Pulser/Receiver to generate and
 203 receive the signals from PPM EMATs, that were used as generator and receiver. The received
 204 signal was acquired by an oscilloscope that was connected to a PC to automate data acquisition.
 205 PPM EMATs were supplied by Sonemat Ltd, with either 10 mm or 6 mm nominal wavelength,
 206 all with a PPM array of 3 cycles (3 pairs of north-south orientated magnets along the length of
 207 the EMAT coil). Fig. 3 shows the experimental setup.



208

209

Fig. 3. Experimental setup

210 The excitation pulse was set to an 8 cycle tone burst at the optimum frequency for each
 211 mode, according to Table I. However, even at the optimum frequency, more than one mode

212 can be generated or received if the dispersion curves of more than one mode intersect the
213 operation region. For instance, in order to generate the SH2 with a 6 mm wavelength EMAT,
214 one has to consider the operating region shown in Fig. 1(b). In this case, not only the intended
215 mode is generated, but also the SH0 and SH1 modes are generated. Mode selection can be
216 refined by adopting dual excitation on both surfaces of the plate [29]. This technique allows
217 generation and reception of only symmetric or antisymmetric modes. Therefore, in the
218 aforementioned example, apart from the SH2 mode, only the SH0 mode would be generated.
219 Further differentiation of modes with the same symmetry was achieved by choosing an optimal
220 receiving position, according to the modes' group velocity, to ensure that unwanted generated
221 modes, or signals from mode conversion with the same symmetry, do not overlap in time.
222 Considering the aforementioned example, since the group velocity of the SH0 and SH2 modes
223 are considerably different, by carefully choosing the distance between the generation position
224 and the discontinuity, distance ℓ_0 in Fig. 2, and the receiver position, either the unwanted
225 generated SH0 mode or scattered waves from this mode can be separated in time. Similarly, by
226 properly choosing the receiving position, one can detect the several modes that can arise due
227 to mode conversion of the intended, SH2, mode without overlapping wave arrivals in time. The
228 same principle applies for generation of the other modes. In this paper, ℓ_0 was set to a distance
229 of between 73 mm to 110 mm, depending on the generated mode. The position of the receiver
230 for direct and reflected waves was set at the left of the transmitter, position (1) in Fig. 2, either
231 at -144 mm or -257 mm. Note that the direct wave could be received at a negative position
232 because the EMAT generates SH waves that travel both forwards and backwards. In order to
233 receive the transmitted waves, the receiver was positioned on the middle of the machined
234 discontinuity, position (2) in Fig. 2. It is worth highlighting that modes with opposite symmetry
235 can arrive at the same time at the receivers, since dual reception method ensures that symmetric
236 and antisymmetric modes can be distinguished. Dual transduction has less restrictive

237 experimental constraints than if a single transducer was used; for instance, shorter plates could
238 be used. Even with dual transduction, generation of the SH0 mode at a 6 mm wavelength would
239 result in excessively complicated interference, with generated and scattered waves needing to
240 be resolved experimentally. At the optimum excitation frequency for the SH0 mode at 6 mm
241 wavelength, the SH2 mode was also generated but with lower group velocity, therefore mixing
242 in time with the scattered waves of interest, without providing a clear receiving position along
243 the plate's length. Thus, the fundamental, SH0 mode was generated only with a nominal 10
244 mm wavelength probe, in order to ensure single mode generation, as shown in Table I; the
245 remaining modes were generated at both 6 mm and 10 mm wavelengths.

246 *3.2. Finite element model*

247 Numerical analysis was performed using a commercial time-domain Finite Element Method
248 (FEM) solver, PZFlex[®], which allows simulation of SH waves in a two-dimensional model.
249 Mirroring the experimental measurements, the symmetric and non-symmetric geometry of Fig.
250 2 were modelled, with aluminium density and transverse wave speed equal to 2698 kg/m³ and
251 $c_T = 3111$ m/s, respectively. In the simulation, the parameter d was varied from 0 to 7.5 mm in
252 0.5 mm steps, in order to analyse the SH interaction as a function of the discontinuity depth
253 more carefully. In order to generate the SH waves, a 3 cycle spatial force distribution function
254 with a period of 10 mm or 6 mm was applied to the surface nodes of the model using a time
255 history that was the same as the excitation current used in the experiment. This approach allows
256 generation of SH guided waves, without the need of including the EMAT in the model, as
257 validated previously elsewhere [3, 10, 29, 32]. Received signals were convolved with a 3 cycle
258 spatial tone burst to simulate the receiving transducer spatial profile. As in the experiments,
259 dual transmission at both surfaces of the plate was adopted to generate the SH guided wave
260 modes.

261 Mode reception could be modelled likewise, replicating the setup used in the experiments.
 262 However, since numerical simulation allows one to access the displacement field for every
 263 point in the plate's cross-section, that is, as a function of y , each mode was effectively separated
 264 from the received signal based on the mode's orthogonality relationship [33-35]. The
 265 displacement profile, given by Eq. (2), forms an orthogonal basis, i.e,

$$\int_{y=-h/2}^{h/2} U_n(y)U_m(y)dy = \begin{cases} 0, & n \neq m \\ C_n, & n = m \end{cases}, \quad (10)$$

266 where

$$C_n = \int_{y=-h/2}^{h/2} U_n(y)U_n(y)dy = \begin{cases} h, & n = 0 \\ h/2, & n \neq 0 \end{cases}. \quad (11)$$

267 As the displacement field in the plate is composed of several SH modes, it can be expressed
 268 as:

$$u(x, y, t) = \sum_{m=0}^N A_m U_m(y) e^{j(\omega t - \kappa_m x)}, \quad (12)$$

269 where $u(x, y, t)$ is the displacement field as a function of x and y coordinates and time, t , and
 270 N is the number of SH modes. Therefore, thanks to the orthogonality relationship of Eq. (10),
 271 one can separate each mode present in the received signal through:

$$u_n(x, t) = \frac{1}{C_n} \int_{y=-h/2}^{h/2} u(x, y, t) U_n(y) dy, \quad (13)$$

272 such that $u_n(x, t)$ is the displacement field of mode n as a function of the longitudinal
 273 coordinate x and time. Normalization by the constant C_n is necessary to provide the proper
 274 dimensions and compensate for the weight of the displacement profile integral.

275 When compared to Lamb waves, the mode profile of SH guided waves is much simpler,
 276 involving a displacement or velocity component only in one direction, meaning that mode
 277 separation based upon the modes' orthogonality can be performed by means of a single field.
 278 Similar processing with Lamb waves [33, 34] requires one to acquire both displacement (or
 279 velocity) and stress in order to use the general orthogonality relationship [28]. In fact, in this
 280 case, the general orthogonality relationship yields Eq. (10), since for SH waves, the relevant
 281 non-zero particle velocity and stress components are scaled versions of the displacement
 282 profile, $U_m(y)$, as seen in Eq.(5) and (6).

283 The accuracy of the numerical computations and mode separation technique was assessed
 284 by calculating the energy balance of the scattered modes. The power of the incident and
 285 scattered modes was computed following Eq. (4): by multiplying the amplitude of the simulated
 286 velocity, v_z , and stress, σ_{xz} , fields of the reflected and transmitted modes as well as the incident
 287 mode, which were separated using the aforementioned post-processing. For the conservation
 288 of energy, the sum of the power of the scattered modes has to be equal to the incident mode's
 289 power. Or, equivalently,

$$1 = \sum_{j=1}^N \frac{P_{ij}^-}{P_i^+} + \sum_{j=1}^N \frac{P_{ij}^+}{P_i^+}, \quad (14)$$

290 where P_{ij}^- and P_{ij}^+ are the power of the reflected and transmitted modes, respectively, of order j
 291 due to the incident mode i , whose power is P_i^+ . The right-hand side of Eq. (14) was calculated
 292 for each incident mode at the simulated discontinuities depths and shapes analysed in this
 293 paper. Results were close to unity, confirming the accuracy of the numerical computations; the
 294 maximum error for each incident mode and discontinuity shape is shown in Table II.

295 **Table 2 Maximum energy balance error in simulations.**

Nominal λ (mm)	Generated mode	Maximum energy balance error (%)	
		Non-Symmetric discontinuity	Symmetric discontinuity

10	SH0	0.70	0.07
	SH1	3.08	1.77
	SH2	2.45	2.59
	SH3	2.69	2.69
6	SH1	1.08	2.47
	SH2	2.11	2.43
	SH3	6.05	4.51

296 *3.3. Reflection and transmission coefficients*

297 The coefficients for reflection from the discontinuity edge, R_{ij} , and transmission to the
 298 discontinuity, T_{ij} , are calculated, in order to perform quantitative analysis of the interaction of
 299 SH guided waves modes with either symmetric or non-symmetric discontinuities. The
 300 subscripts i and j in the coefficient notation represents the incident and received mode orders
 301 respectively. These coefficients are formally defined by:

$$R_{ij} = \frac{A_j^{(1)-}}{A_i^{(1)+}}, \quad (15)$$

$$T_{ij} = \frac{A_j^{(2)+}}{A_i^{(1)+}} \sqrt{\frac{h-d}{h}}, \quad (16)$$

302 where A is the maximum peak-to-peak amplitude of the received signal, the superscripts “+”
 303 and “-” mean the forward and backward propagating waves, respectively. The superscripts (1)
 304 and (2) indicate the reading positions: before the thinner region edge and on the thinner region,
 305 respectively, as shown in Fig. 2. Here, i and j can be 0 to 3, corresponding to the SH0 to SH3
 306 modes, respectively. The square root in Eq. (16) is included to compensate for the natural
 307 amplitude increase of a wave when it is transmitted into a thinner region of the plate.

308 In order to calculate the coefficients, a time gate in which the forward or backward waves
 309 are expected to arrive was defined for each mode according to the receiving position, tone burst
 310 time duration and group velocity of the modes. When the thinner region remaining thickness
 311 is below the mode cut-off thickness, its group velocity is not a real number and thus a time gate

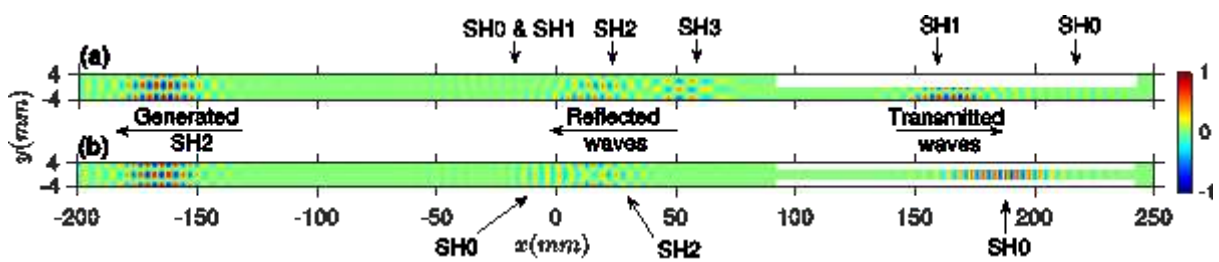
312 for T_{i1} , T_{i2} or T_{i3} cannot be defined. Experimental and numerical signals were treated differently
313 in this case. Experimental transmission coefficients were not calculated, because without a
314 well-defined time gate, one cannot properly select the pulse relative to each mode. No time
315 gate restriction was applied to calculate numerical coefficients since the several modes can be
316 effectively separated through Eq. (13). This was done in order to allow analysis of any residual
317 component inside the thinner section, when the cut-off thickness is exceeded. The same
318 approach was applied to reflection coefficients of modes that cannot propagate in the original
319 thickness section, dash marks in Table I.

320 In the interest of having meaningful values of the coefficients, compensation for amplitude
321 reduction due to attenuation and mode dispersion was necessary. Compensation was performed
322 by calculating the amplitude decay rate per propagated length in a non-machined plate for each
323 generated mode, which was then used to compensate the amplitude of the received signals,
324 considering the propagated distance at the receiving point. The propagated distance includes
325 the forward and backward path, in the case of the reflection coefficient. When considering
326 mode conversion, the compensation considered the proper mode in each part of the propagation
327 path. For instance, when calculating the coefficient R_{21} , compensation should consider the
328 mode SH2 along the forward path and the mode SH1 along the backward path. The only
329 mechanism for amplitude decrease in the numerical simulation is pulse spreading due to
330 dispersion since no damping was introduced in the simulation. Therefore, different
331 compensating factors were used for experimental and numerical data. Nevertheless, once
332 compensated, the coefficients could be straightforwardly compared.

333 **4. Results**

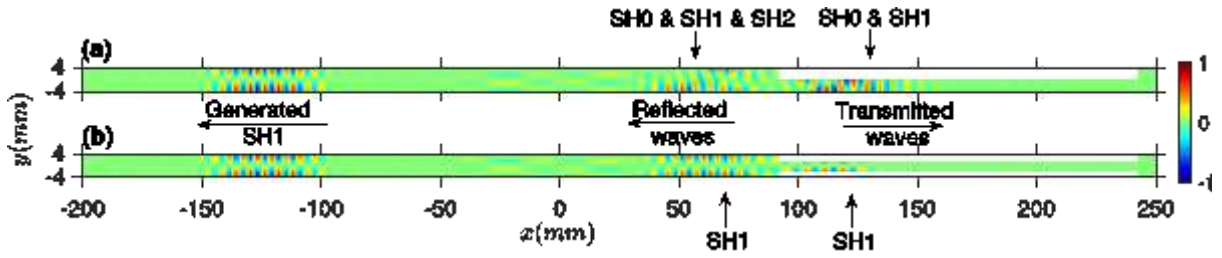
334 Fig. 4 (a) and (b) show a snapshot of the simulated particle velocity field due to the
335 generation of the symmetric SH2 mode at 6 mm wavelength, in an 8 mm thick aluminium plate

336 with 4 mm deep non-symmetric and symmetric discontinuities, respectively. The SH2 mode is
 337 generated at the origin and propagates to the left and the right. The wave propagating to the left
 338 is seen around -160 mm, which clearly shows the SH2 symmetric structure across the plate
 339 thickness. The wave propagating to the right interacts with the discontinuity, being mode
 340 converted to several modes, either as reflection or transmission into the discontinuity, which
 341 are indicated in Fig. 4. The wave structures of the SH3 and SH2 modes are clearly seen among
 342 the reflected waves at the non-symmetric discontinuity in Fig. 4(a). Moreover, the SH0 and
 343 SH1 modes can also be seen, mixed and ahead of the other modes due to their higher group
 344 velocity. The SH0 and SH1 modes are transmitted to the thinner region, where higher order
 345 modes cannot propagate due to their cut-off thickness (see Table I). Examining Fig. 4(b), one
 346 clearly sees that the interaction with a symmetric discontinuity differs from the non-symmetric
 347 case; there is mode conversion, either as reflection or transmission, uniquely to symmetric
 348 modes. Fig. 5 shows the wave field for the generation of the SH1 mode at 6 mm wavelength.
 349 In this case, since the incident mode is antisymmetric, the interaction with a symmetric
 350 discontinuity [Fig. 5(b)] allows mode conversion to antisymmetric modes only, whereas when
 351 the discontinuity is non-symmetric [Fig. 5(a)] all types of SH modes can be mode converted.



352

353 Fig. 4. Normalized particle velocity at 75 μ s for a plate with 4 mm deep (a) non-symmetric and (b) symmetric
 354 discontinuity for generation of the SH2 mode at the origin.



355

356 Fig. 5. Normalized particle velocity at $50 \mu\text{s}$ for a plate with 4 mm deep (a) non-symmetric and (b) symmetric
 357 discontinuity for generation of the SH1 mode at the origin.

358

359 Fig. 6 and Fig. 7 show the numerical and experimental received signals at -257 mm ,

360 with the origin set at $\ell_0 = 92 \text{ mm}$, due to the generation of the SH2 mode at 6 mm wavelength

361 interacting with 4 mm deep non-symmetric and symmetric discontinuities, respectively. The

362 separated symmetric and antisymmetric parts of the experimental signals are shown in plots (a)

363 and (b), respectively, whereas the numerical signals are shown in plots (c) and (d) in Fig. 6 and

364 Fig. 7. The generated mode prior to interacting with the discontinuity is observable between

365 100 and 120 μs in plots (a) and (c), whereas the other wave packets correspond to the reflected

366 waves from the discontinuity. Experimental signals have lower amplitude than simulated ones,

367 as damping was not included in the simulation, and normalization was performed considering

368 the direct wave that was not mode-converted. Considering the non-symmetric discontinuity

369 (Fig. 6), the symmetric modes, SH2 and SH0, are received, around 180 μs and 150 μs ,

370 respectively, in Fig. 6(a). These modes can be separated in time due to the different group

371 velocities, but the extent to which they can be clearly separated does depend on the receiving

372 position: generally SH0 and SH2 may overlap in time, hindering identification. In fact, the

373 reflected SH0 mode arrives between the direct SH2 signal and the reflected SH2 signal, as this

374 receiving position was carefully chosen for this purpose. In this position one can also

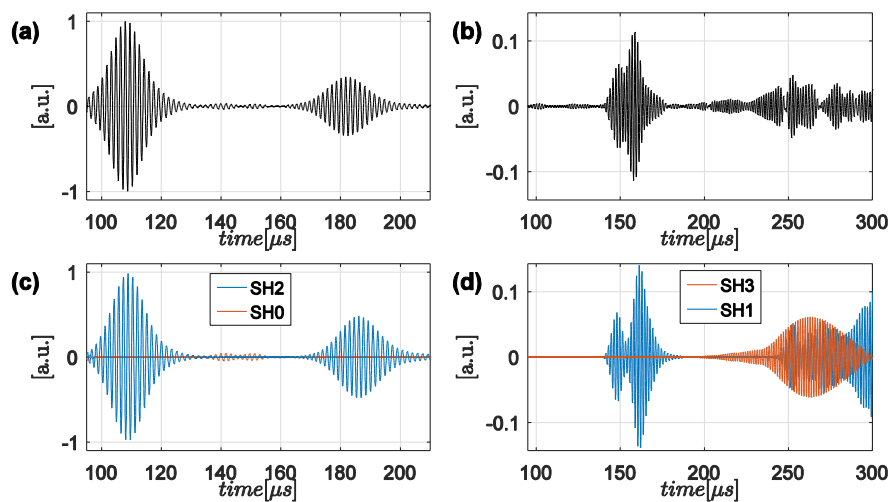
375 distinguish the antisymmetric modes, Fig. 6 (b) and (d). The SH1 mode arrives at around 160

376 μs and is clearly identified. The SH3 mode, on the other hand, is not clearly resolved in time;

377 due to its low group velocity, it was expected to arrive at approximately 250 μs , being mixed

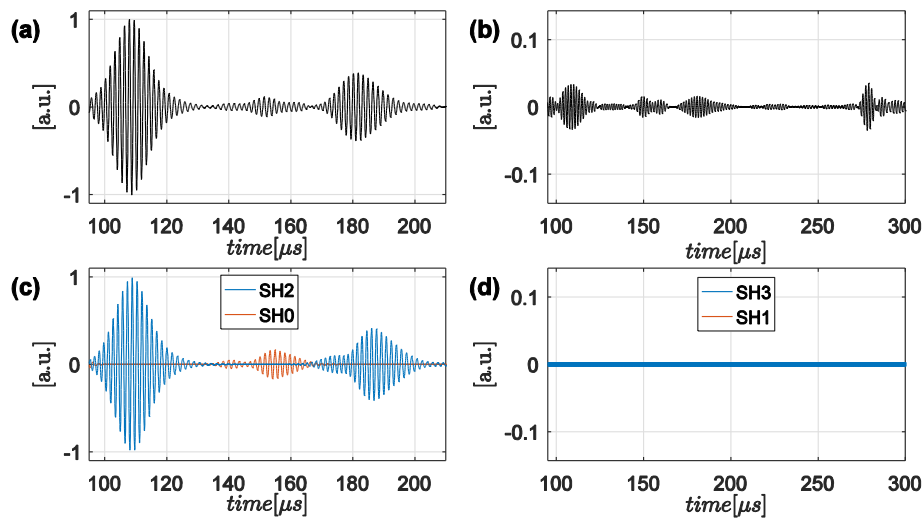
378 with the reflected SH1 mode from the leftmost end of the plate, resulting in a complicated
 379 interfered signal. Therefore, this position is not ideal for clearly detecting this mode
 380 experimentally; indeed, a position closer to origin was chosen in order to properly calculate
 381 this mode amplitude without mode mixing. A cleaner mode separation is achieved within the
 382 numerically simulated signal by decomposition into the orthogonal basis, using Eq. (13). The
 383 separated signals are shown in Figs. 6 (c) and (d), where the individual modes are effectively
 384 separated even when they overlap.

385 The signals arising due to the interaction with a symmetric discontinuity are shown in
 386 Fig. 7, where one can see that the amplitude of the reflected SH0 modes is increased [Fig. 7 (a)
 387 and (b)], but mainly that signals associated with the antisymmetric modes have vanished [Fig.
 388 7 (b) and (d)]. The low amplitude, experimental antisymmetric signal in Fig. 7(b) is due to the
 389 inherent imprecision of the experimental mode selectivity procedure, which is higher for
 390 selecting modes with opposite symmetry to the generated one [29], and is also possibly due to
 391 machining imprecision, which could result in a real discontinuity that is not perfectly
 392 symmetric. The highest difference between the depths of the machined discontinuities in both
 393 surfaces was measured at 0.13 mm which implies in about 6% of maximum symmetry error.



394

395 Fig. 6. Received signals at $x = -257$ mm due to the generation of SH2 at the origin interacting with a non-symmetric
 396 4mm deep discontinuity starting at $x=92$ mm. Experimental signals (a) and (b) and numerical signals (c) and (d).
 397 Symmetric modes (a) and (c) and antisymmetric modes (b) and (d).



399

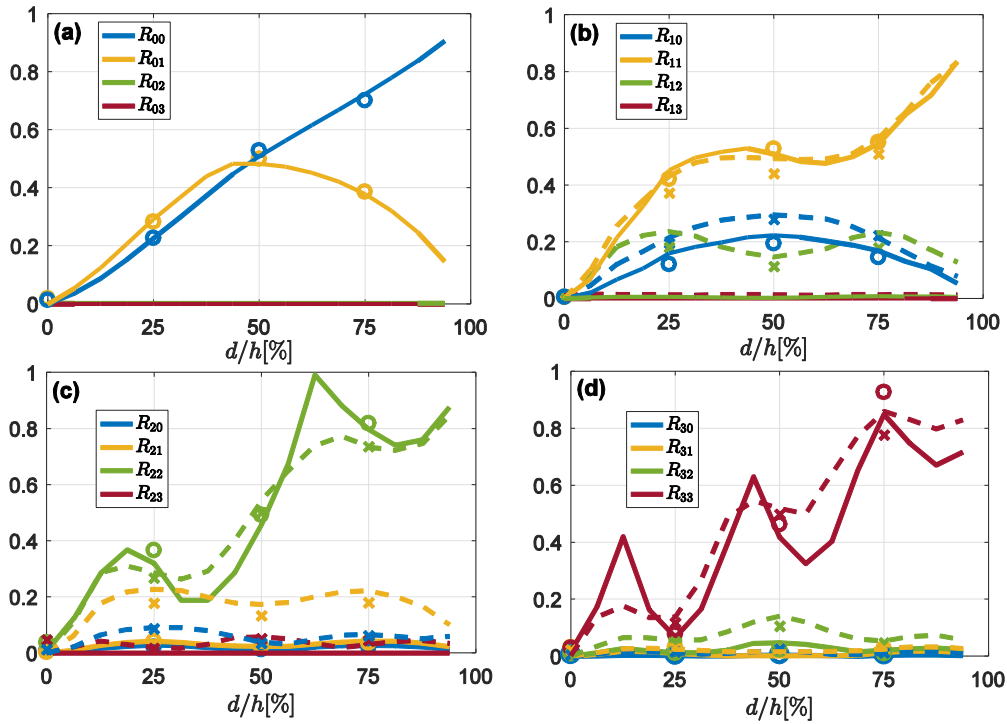
400 Fig. 7. Received signals at $x = -257$ mm due to the generation of SH2 at the origin interacting with a symmetric
 401 4mm deep discontinuity starting at $x=92$ mm. Experimental signals (a) and (b) and numerical signals (c) and (d).
 402 Symmetric modes (a) and (c) and antisymmetric modes (b) and (d).

403 The wave field in Fig. 4 and Fig. 5 and the experimental signals in Fig. 6 and Fig. 7
 404 show that for a symmetric discontinuity, mode conversion occurs exclusively to modes with
 405 the same symmetry as the incident one, whereas all modes can be mode converted due to the
 406 interaction with a non-symmetric discontinuity. Theoretically, this happens because a
 407 symmetric discontinuity presents identical boundary conditions in both surfaces of the plate,
 408 therefore imposing that the scattered field in both halves of the plate behaves equally with
 409 respect to the plate's mid-plane, which consequently restricts mode-conversion within the same
 410 type of symmetry of the incident mode. On the other hand, in a non-symmetric discontinuity,
 411 there is no symmetry on the boundary conditions and therefore, any mode-conversion is
 412 allowed. Also, the intensity of the reflected and transmitted modes differs in both cases,
 413 depending on whether the discontinuity is symmetric or non-symmetric. In order to perform
 414 further analysis, quantitative data is obtained by calculating the reflection and transmission
 415 coefficients, according to Eqs. (15) and (16), respectively. The reflection coefficients due to
 416 non-symmetric and symmetric discontinuities as a function of the discontinuity depth are
 417 shown in Fig. 8 and Fig. 9, respectively. Experimental and numerical data for 10 mm and 6

418 mm nominal wavelengths are shown. Solid lines and circles represent signals obtained with a
419 transducer of 10 mm wavelength, either numerically or experimentally, respectively. Dashed
420 lines and crosses represent results for the 6 mm wavelength transducer, either numerically or
421 experimentally, respectively.

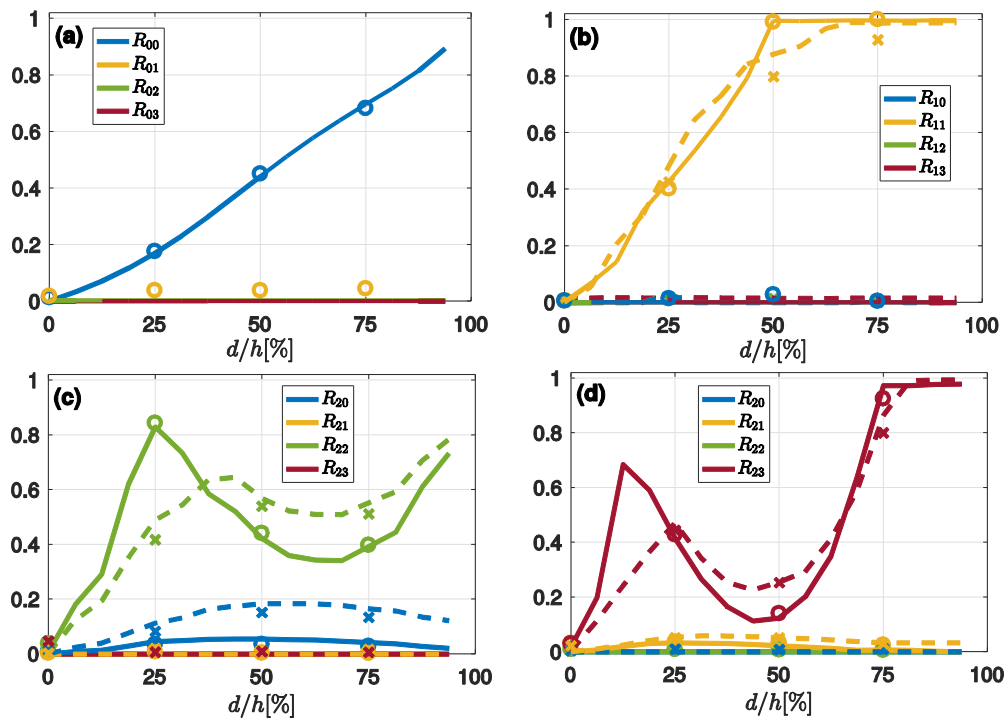
422 Incident symmetric modes, either the SH0 or SH2 modes, are shown in plots (a) and
423 (c), respectively. One can clearly see that for the symmetric discontinuity, Fig. 9(a) and (c),
424 there is mode conversion uniquely to symmetric modes, whereas all modes can potentially be
425 mode converted due to the interaction with a non-symmetric discontinuity, Fig. 8 (a) and (c).
426 This experimentally confirms the numerical results of Pau et al. [17, 19], who analysed the
427 incident SH0 mode. The coefficients for incident antisymmetric modes, either the SH1 or SH3,
428 are shown in plots (b) and (d), respectively. In this case, a symmetric discontinuity leads only
429 to antisymmetric modes arising from mode conversion. As shown in Table I, at the optimum
430 excitation frequency and wavelength used to generate each of the SH modes, not all of the other
431 modes can propagate due to their cut-off thickness. Accordingly, only conversions to the
432 predicted allowed modes were experimentally and numerically detected in Fig. 8 and Fig. 9.
433 The intensity of the converted modes is higher with a wavelength of 6 mm than a wavelength
434 of 10 mm, because the dispersion curves of the shorter wavelength guided waves are closer to
435 each other in the frequency-phase velocity plane. Therefore, converted modes are received with
436 higher intensity due to the finite operating region [see Fig. 1(b)].

437



438

439 Fig. 8. Numerical (lines) and experimental (symbols) reflection coefficient versus discontinuity depth for a non-
 440 symmetric discontinuity due to incident (a) SH0, (b) SH1, (c) SH2 and (d) SH3. Solid lines and circles represent
 441 transducer wavelength of 10 mm and dashed lines and crosses represent 6 mm transducer wavelength.



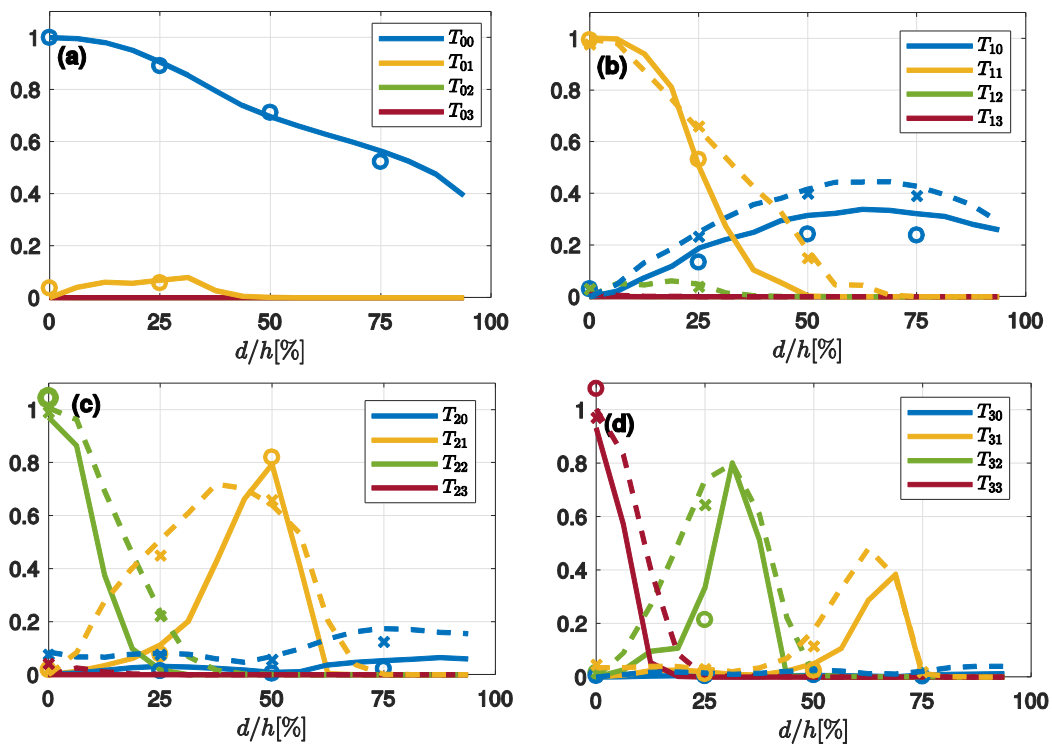
442

443 Fig. 9. Numerical (lines) and experimental (symbols) reflection coefficient versus discontinuity depth for a
 444 symmetric discontinuity due to incident (a) SH0, (b) SH1, (c) SH2 and (d) SH3. Solid lines and circles represent
 445 transducer wavelength of 10 mm and dashed lines and crosses represent 6 mm transducer wavelength.

446

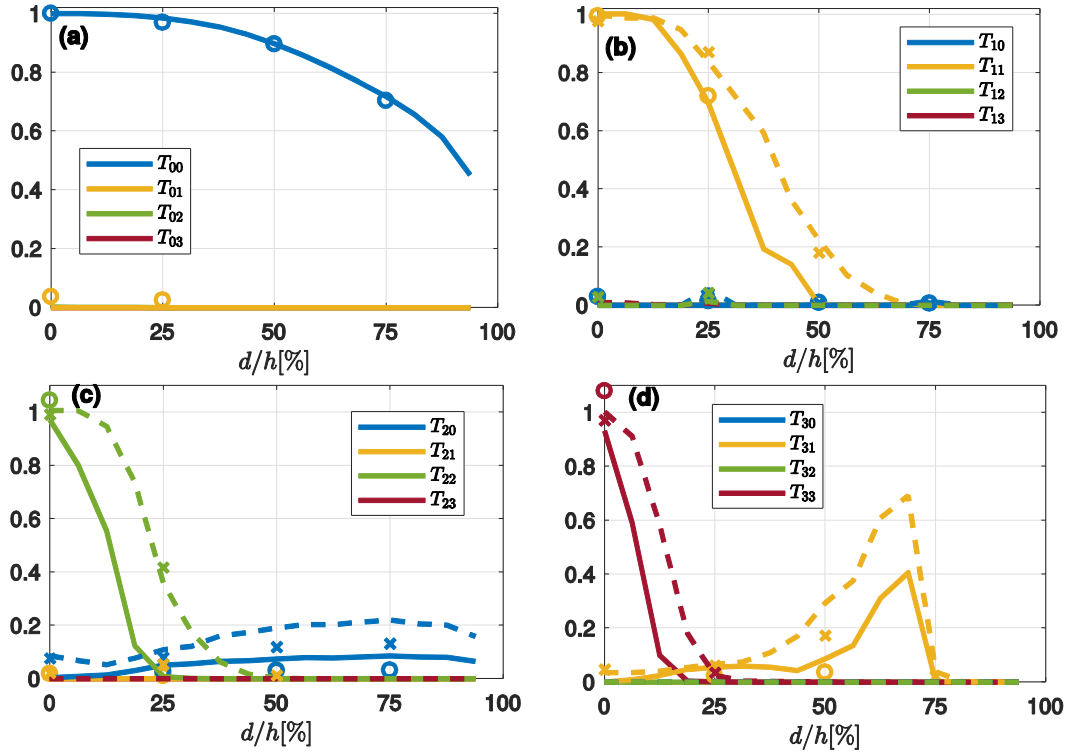
447 The transmission coefficient due to non-symmetric and symmetric discontinuity is shown
 448 in Fig. 10 and Fig. 11, respectively. Due to the mode cut-off thickness, transmission coefficient
 449 to non-fundamental modes must eventually tend to zero as the discontinuity depth increases.
 450 This behaviour can be verified in Fig. 10 and Fig. 11, and the relative depths in which the
 451 coefficients approach zero correspond to the ones theoretically calculated in Table I, either for
 452 10 mm or 6 mm wavelengths. The same mode conversion behaviour regarding the
 453 discontinuity symmetry is valid for the transmitted waves; i.e., within a symmetric
 454 discontinuity there can be mode conversion to modes that share the same symmetry condition
 455 as the incident modes, either symmetric or antisymmetric. Generally, numerical and
 456 experimental data show good agreement.

457



458

459 Fig. 10. Numerical (lines) and experimental (symbols) transmission coefficient versus discontinuity depth for a
 460 non-symmetric discontinuity due to incident (a) SH0, (b) SH1, (c) SH2 and (d) SH3. Solid lines and circles
 461 represent transducer wavelength of 10 mm and dashed lines and crosses represent 6 mm transducer wavelength.



462

463 Fig. 11. Numerical (lines) and experimental (symbols) transmission coefficient versus discontinuity depth for a
 464 symmetric discontinuity due to incident (a) SH0, (b) SH1, (c) SH2 and (d) SH3. Solid lines and circles represent
 465 transducer wavelength of 10 mm and dashed lines and crosses represent 6 mm transducer wavelength.

466 5. Discussion

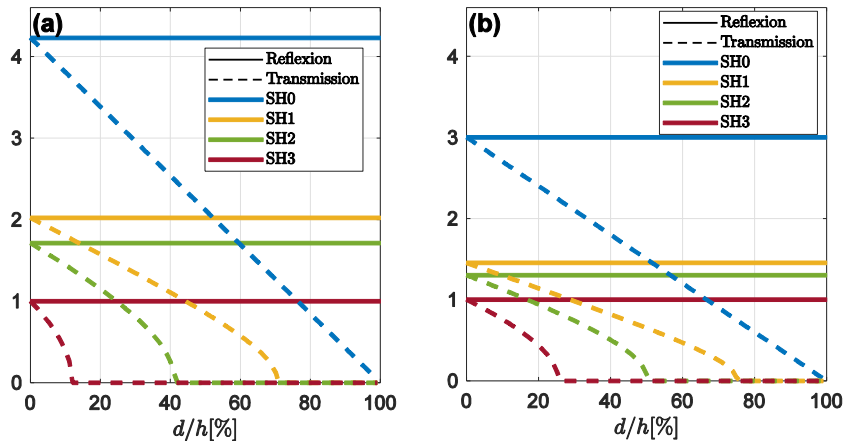
467 Previous work [20] has shown that the coefficients for incident SH0 and SH1 modes,
 468 in a frequency-thickness product value in which only these two modes can propagate, behave
 469 non-monotonically, unlike at the low frequency-thickness value, where coefficients are
 470 monotonic [16, 24]. Here, higher order modes were used as incident modes, and it is observed
 471 that the higher the order of the generated mode, the more intense the non-monotonic behaviour
 472 of the coefficients is. In Fig. 8, the R_{00} coefficient shows a linear behaviour whereas, R_{11}
 473 presents a zero derivative point for around half thickness discontinuity with 6 mm wavelength,
 474 and one local maximum point with 10 mm wavelength, and R_{22} and R_{33} show two and three
 475 local maxima points, respectively. The peaks in the reflection coefficient occur at discontinuity
 476 depths that correspond to the remaining thicknesses being slightly higher than the cut-off
 477 thicknesses of the SH modes. One should also note that for a larger generated wavelength,

478 where the operating frequency is closer to the mode cut-off frequency-thickness and dispersion
479 is at its highest [see Fig. 1(b)], the non-monotonicity is yet more acute, i.e. the peaks and
480 troughs are more well defined, as it can be seen comparing the solid and dashed lines for R_{22}
481 and R_{33} in Fig. 8 (c) and (d). Interestingly for symmetric discontinuities, the non-monotonic
482 behaviour is less accentuated, typically with fewer oscillations (see Fig. 9).

483 The values for the reflection and transmission coefficients, observed in Figs. 8 to 11, are a
484 consequence of the boundary condition at the discontinuity and the energy conservation
485 principle. Some of the interesting behaviour as a function of the discontinuity depth can be
486 explained from consideration of ultrasonic energy or power. The incident mode carries energy
487 which is proportional to its power level, E_n , defined in Eq.(9). Note that E_n , does not include
488 the amplitude of the mode, the power is given by Eq.(8), in which E_n is multiplied by the square
489 of displacement amplitude. At a fixed frequency, a high-order mode has higher phase velocity,
490 (see Fig. 1(b)), and consequently lower wavenumber and, therefore, a lower power level (see
491 Eq.(9)) than the other possible propagating modes. Since the energy of the incident mode has
492 to be redistributed among the scattered modes, one can expect that the amplitude of a scattered
493 high-order mode should be higher than that of a lower-order mode, since the latter has a higher
494 power level. Fig. 12(a) shows the power level of the reflected and transmitted SH modes
495 normalized per the power level of the incident SH3 at 662 kHz, calculated from Eq.(9),
496 considering the actual wavenumber value inside the discontinuity. Following this reasoning,
497 the values of the reflection and transmission coefficients to higher-order modes are expected
498 to be higher than those to lower-order modes. Taking, for instance, the SH3 as the incident
499 mode, when the discontinuity is shallow, energy balance is almost completely satisfied by a
500 high transmission coefficient to the same-order mode, i.e., the SH3 mode, as can be seen in
501 Fig. 10(d). As the depth increases, this mode's cut-off thickness is approached to a point at
502 which it can no longer propagate, i.e. it carries no energy. Simultaneously, the amplitude of the

503 reflected SH3 mode increases until reaching a peak [Fig. 8(d)], when the thickness of the
504 thinner section is equal to this mode cut-off thickness. When the discontinuity depth increases
505 further, the power level of the SH2 mode inside the thinner section decreases, approaching the
506 power level of the incident SH3 mode, (see Fig.12.(a) at about $20\% < d/h < 40\%$), because
507 its wavenumber decreases in the thinner section - recall that its phase velocity increases for a
508 lower thickness [11]. Thus the transmission of the SH2 mode is maximized [Fig. 10(d)] and
509 the reflection of the SH3 mode decreases [Fig. 8(d)]. If discontinuity depth keeps increasing,
510 the SH2 mode can no longer propagate inside the thinner section, and reflection of the SH3
511 mode again reaches a peak [Fig. 8(d)]. This also happens for the SH1 mode, in the
512 discontinuity, Fig.12.(a) at about $40\% < d/h < 70\%$. This mechanism of preferred energy
513 swapping between reflection to the same-order mode and transmission to the highest order
514 mode that is able to propagate in the thinner section, therefore explains the occurrence of peaks
515 in the reflection and transmission coefficients in the same quantity as the order of the incident
516 mode, observed in Fig. 8.

517 For symmetric discontinuities, the same principle holds if skipping consecutive modes,
518 since only modes that share the same symmetry as the incident mode can be created in this
519 case. Therefore, it is expected that the peaks for the reflection of the same-order mode to be
520 even higher. Following the example for the incident SH3 mode, when its transmission is no
521 longer possible, because the thickness of the thinner region is less than its cut-off thickness,
522 then the reflection of the SH3 mode should be even stronger. The antisymmetric mode with the
523 closest power level is the SH1 mode, whose power level is elevated [see Fig.12(a)], and thus
524 would have a lower amplitude. The higher values for the peaks within a symmetric
525 discontinuity can be verified comparing Fig.9(d) and Fig.8(d).



526

527 **Figure 12** Power level for reflected (solid lines) and transmitted (dashed) modes normalized per the power level of the
 528 incident SH3 mode at (a) 662 kHz and (b) 782 kHz as a function of the discontinuity depth. The power level of a
 529 transmitted mode reaches zero at its respective cut-off thickness.

530 When a higher-order mode is generated at a lower wavelength, and consequently, higher
 531 wavenumber, its power level is closer to the other modes, see Fig. 12.(b), and therefore, the
 532 intensity of scattered modes is more equally distributed. Consequently, the difference between
 533 peaks and valleys in the reflection coefficient is less accentuated, since the aforementioned
 534 preferred energy swap mechanism is no longer valid, as more modes significantly participate
 535 in the energy redistribution.

536 The peaks in the reflection coefficient of higher-order modes could suggest interesting
 537 applications in NDT, if a higher amplitude reflection from a shallow discontinuity of a specific
 538 critical value is intended. For instance, a possible application would be to detect the presence
 539 of a defect of a specific depth or to monitoring the growth of a discontinuity. In this potential
 540 application, one would set the operating wavelength and frequency close to the cut-off
 541 frequency and the resulting cut-off thickness should match the remaining thickness that
 542 corresponds to a critical depth of interest. When the discontinuity depth approaches the critical
 543 value an intense reflection is received, facilitating detection.

544 **6. Conclusion**

545 The interaction of fundamental and higher-order SH guided wave modes with symmetric
546 and non-symmetric thickness discontinuities in plates was experimentally and numerically
547 analysed through quantitative data. Experimentally, generation and receiving positions had to
548 be chosen carefully, to avoid mode mixing. Dual transduction helps to avoid mode mixing by
549 separating symmetric and antisymmetric modes. Numerically, an orthogonal mode
550 decomposition, post-processing method allowed effective mode separation.

551 It was experimentally confirmed that mode conversion depends not only on the thinning
552 depth but also on its symmetry. All possible mode conversions can occur in non-symmetric
553 discontinuities, whereas only mode conversion to modes with the same type of symmetry of
554 the incident mode can happen due to the interaction with a symmetric discontinuity. The
555 investigation of incident higher-order modes also revealed that the reflection coefficient of
556 higher-order modes present even stronger non-monotonicity as a function of the discontinuity
557 depth, which is reduced when the discontinuity is symmetric. Additionally, one can conclude
558 that at a lower frequency, closer to the cut-off frequency of the incident mode, the behaviour
559 of the reflection and transmission coefficients presents yet more accentuated variations over
560 the discontinuity depth range. There are peaks in the reflection coefficient of the same mode as
561 the incident one, and in the transmission coefficient to lower-order modes at discontinuity
562 depths that correspond to remaining thicknesses close to the cut-off thicknesses. This behaviour
563 is explained by consideration of the proposed mechanism based on the energy conservation
564 principle.

565 This paper's results further elucidate the interaction of SH guided waves with a thickness
566 discontinuity section. The different behaviour between symmetric and non-symmetric
567 discontinuities was experimentally demonstrated, also showing that the behaviour of higher-

568 order SH modes is yet more complex and highly dependent not only on the discontinuity depth
569 but also on its positioning in the plate's cross-section and on the frequency.

570

571 Acknowledgements

572 Authors would like to thank the Brazilian National Council for Scientific and Technological
573 Development, CNPq, for financial support.

574 References

- 575 [1] M. Hirao and H. Ogi, "An SH-wave EMAT technique for gas pipeline inspection," *NDT & E*
576 *International*, vol. 32, no. 3, pp. 127-132, 1999/04/01/ 1999
- 577 [2] S. Dixon, S. E. Burrows, B. Dutton, and Y. Fan, "Detection of cracks in metal sheets using pulsed laser
578 generated ultrasound and EMAT detection," *Ultrasonics*, vol. 51, no. 1, pp. 7-16, 2011.
- 579 [3] M. Clough, M. Fleming, and S. Dixon, "Circumferential guided wave EMAT system for pipeline
580 screening using shear horizontal ultrasound," vol. 86, pp. 20-27, 2017.
- 581 [4] Nurmalia, N. Nakamura, H. Ogi, and M. Hirao, "EMAT pipe inspection technique using higher mode
582 torsional guided wave T(0,2)," *NDT & E International*, vol. 87, pp. 78-84, 2017/04/01/ 2017.
- 583 [5] Y. Shen and V. Giurgiutiu, "Combined analytical FEM approach for efficient simulation of Lamb wave
584 damage detection," *Ultrasonics*, vol. 69, pp. 116-128, 2016/07/01/ 2016.
- 585 [6] R. Carandente, J. Ma, and P. Cawley, "The scattering of the fundamental torsional mode from axi-
586 symmetric defects with varying depth profile in pipes," (in eng), *J Acoust Soc Am*, vol. 127, no. 6, pp.
587 3440-8, Jun 2010.
- 588 [7] Nurmalia, N. Nakamura, H. Ogi, M. Hirao, and K. Nakahata, "Mode conversion behavior of SH guided
589 wave in a tapered plate," vol. 45, no. 1, pp. 156-161, 2012.
- 590 [8] R. Carandente and P. Cawley, "The effect of complex defect profiles on the reflection of the fundamental
591 torsional mode in pipes," *NDT & E International*, vol. 46, pp. 41-47, 2012/03/01/ 2012.
- 592 [9] S. Dixon, P. A. Petcher, Y. Fan, D. Maisey, and P. Nickolds, "Ultrasonic metal sheet thickness
593 measurement without prior wave speed calibration," *Journal of Physics D: Applied Physics*, vol. 46, no.
594 44, p. 445502, 2013.
- 595 [10] P. A. Petcher, S. E. Burrows, and S. Dixon, "Shear horizontal (SH) ultrasound wave propagation around
596 smooth corners," vol. 54, no. 4, pp. 997-1004, 2014.
- 597 [11] W. Luo and J. L. Rose, "Guided wave thickness measurement with EMATs," *Insight - Non-Destructive*
598 *Testing and Condition Monitoring*, vol. 45, no. 11, pp. 735-739, // 200.
- 599 [12] A. Demma, P. Cawley, and M. Lowe, "Scattering of the fundamental shear horizontal mode from steps
600 and notches in plates," *The Journal of the Acoustical Society of America*, vol. 113, no. 4, pp. 1880-1891,
601 2003.
- 602 [13] A. Demma, P. Cawley, M. Lowe, and A. G. Roosenbrand, "The reflection of the fundamental torsional
603 mode from cracks and notches in pipes," *The Journal of the Acoustical Society of America*, vol. 114, no.
604 2, pp. 611-625, 2003.
- 605 [14] A. Demma, P. Cawley, M. Lowe, A. G. Roosenbrand, and B. Pavlakovic, "The reflection of guided
606 waves from notches in pipes: a guide for interpreting corrosion measurements," *NDT & E International*,
607 vol. 37, no. 3, pp. 167-180, 2004/04/01/ 2004.
- 608 [15] H. Nurmalia and Nobutomo Nakamura and Hirotsugu Ogi and Masahiko, "Detection of Shear Horizontal
609 Guided Waves Propagating in Aluminum Plate with Thinning Region," *Japanese Journal of Applied*
610 *Physics*, vol. 50, no. 7S, p. 07HC17, 2011.
- 611 [16] D. Achillopoulou, A. Pau, and F. Vestroni, *Damage characterization in waveguides with ultrasonic*
612 *shear waves*. 2015.
- 613 [17] A. Pau, D. V. Achillopoulou, and F. Vestroni, "Scattering of guided shear waves in plates with
614 discontinuities," *NDT & E International*, vol. 84, pp. 67-75, 2016/12/01/ 2016.

- 615 [18] P. Rajagopal and M. J. S. Lowe, "Scattering of the fundamental shear horizontal guided wave by a part-
616 thickness crack in an isotropic plate," *The Journal of the Acoustical Society of America*, vol. 124, no. 5,
617 pp. 2895-2904, 2008.
- 618 [19] A. Pau and D. V. Achillopoulou, "Interaction of Shear and Rayleigh-Lamb Waves with Notches and
619 Voids in Plate Waveguides," (in eng), *Materials (Basel)*, vol. 10, no. 7, Jul 2017.
- 620 [20] A. C. Kubrusly, M. A. Freitas, J. P. von der Weid, and S. Dixon, "Interaction of SH guided waves with
621 wall thinning," *NDT & E International*, vol. 101, pp. 94-103, 2019/01/01/ 2019
- 622 [21] J. Combaniere, P. Cawley, K. McAughey, and J. Giese, "Interaction Between SH₀ Guided Waves and
623 Tilted Surface-Breaking Cracks in Plates," *IEEE Transactions on Ultrasonics, Ferroelectrics, and*
624 *Frequency Control*, vol. 66, no. 1, pp. 119-128, 2019.
- 625 [22] J. Ma and P. Cawley, "Low-frequency pulse echo reflection of the fundamental shear horizontal mode
626 from part-thickness elliptical defects in plates," (in eng), *J Acoust Soc Am*, vol. 127, no. 6, pp. 3485-93,
627 Jun 2010.
- 628 [23] R. Carandente, A. Lovstad, and P. Cawley, "The influence of sharp edges in corrosion profiles on the
629 reflection of guided waves," *NDT & E International*, vol. 52, pp. 57-68, 2012/11/01/ 2012.
- 630 [24] S. Wang, S. Huang, W. Zhao, and Z. Wei, "3D modeling of circumferential SH guided waves in pipeline
631 for axial cracking detection in ILI tools," *Ultrasonics*, vol. 56, pp. 325-331, 2015/02/01/ 2015.
- 632 [25] Y. Ho Cho, J. L. Rose, and H. Geon Kwun, "SH Guided Wave Scattering in a Structure with Thickness
633 Variation," vol. 321-323, pp. 792-794, 2006.
- 634 [26] L. Moreau, A. Velichko, and P. D. Wilcox, "Accurate finite element modelling of guided wave scattering
635 from irregular defects," *NDT & E International*, vol. 45, no. 1, pp. 46-54, 2012/01/01/ 2012.
- 636 [27] H. Nurmalia and Nobutomo Nakamura and Hirotsugu Ogi and Masahiko, "Mode Conversion and Total
637 Reflection of Torsional Waves for Pipe Inspection," *Japanese Journal of Applied Physics*, vol. 52, no.
638 7S, p. 07HC14, 2013.
- 639 [28] X. Yan and F.-G. Yuan, "A semi-analytical approach for SH guided wave mode conversion from
640 evanescent into propagating," *Ultrasonics*, vol. 84, pp. 430-437, 2018/03/01/ 2018.
- 641 [29] A. Kubrusly, M. d. A. Freitas, J. P. von der Weid, and S. Dixon, "Mode selectivity of SH guided waves
642 by dual excitation and reception applied to mode conversion analysis.," *Ultrasonics, Ferroelectrics and*
643 *Frequency Control, IEEE Transactions on*, vol. to be published, 2018.
- 644 [30] J. L. Rose, *Ultrasonic Guided waves in solid media*. Cambridge University Press, 2014.
- 645 [31] B. A. Auld, *Acoustic fields and waves in solids*, 2nd ed. ed. Malabar, Fla.: R.E. Krieger, 1989.
- 646 [32] P. A. Petcher and S. Dixon, "Mode mixing in shear horizontal ultrasonic guided waves," *Nondestructive*
647 *Testing and Evaluation*, pp. 1-20, 2016.
- 648 [33] G. Shkerdin and C. Glorieux, "Lamb mode conversion in a plate with a delamination," *The Journal of*
649 *the Acoustical Society of America*, vol. 116, no. 4, pp. 2089-2100, 2004/10/01 2004.
- 650 [34] L. Moreau, M. Castaings, B. Hosten, and M. V. Predoi, "An orthogonality relation-based technique for
651 post-processing finite element predictions of waves scattering in solid waveguides," *The Journal of the*
652 *Acoustical Society of America*, vol. 120, no. 2, pp. 611-620, 2006/08/01 2006.
- 653 [35] X. Yan and F.-G. Yuan, "Conversion of evanescent Lamb waves into propagating waves via a narrow
654 aperture edge," *The Journal of the Acoustical Society of America*, vol. 137, no. 6, pp. 3523-3533,
655 2015/06/01 2015.